41st AIAA Fluid Dynamics Conference and Exhibit
27 - 30 June 2011, Honolulu, Hawaii

AIAA 2011-3707

DNS of strong shock and turbulence interactions including real gas effects

Xiaowen Wang* and Xiaolin Zhong #1
Mechanical and Aerospace Engineering Department
University of California, Los Angeles, CA 90095

Abstract

The underlying physics in strong shock and turbulence interaction is essential for better understanding of many applications in astrophysics as well as explosive processes. These strongly nonlinear phenomena, however, have proven to be very complex to understand with existing tools. Furthermore, real gas effects including internal energy excitations, translation-vibration energy relaxation, and chemical reactions among different species need to be considered in direct numerical simulation (DNS) of strong shocks, because gas temperature increases dramatically behind the shocks. To solve such problems, a unique approach of using a shock-fitting and shock-capturing method is adopted. The main shock is treated by a shock-fitting method as a sharp boundary of the computational domain. The rest of weak or secondary shocks induced by interactions of the main shock and freestream turbulence are captured by shock-capturing schemes. In this paper, a high-order nonequilibrium flow solver based on 5-species air chemistry and recently thermal property models are implemented and tested. The test of 11-species air chemistry is ongoing, where the ionization of gas particles is considered. The solver is being applied to simulate strong shock and turbulence interaction problems with the main shock Mach number around 20. The paper mainly focuses on the numerical method and results of a test case.

1. Introduction

Many important scientific and engineering applications involve complex interactions between strong shock and turbulent flow. Very high rates of compression and expansion waves are observed in a number of astrophysical applications as well as explosive phenomena such as volcanic eruptions, detonations, shock wave lithotripsy to break up kidney stones, supernova explosion, as well as the implosion of a cryogenic fuel capsule for inertial confinement fusion (ICF). The underlying physics in strong shock and turbulence interaction is essential for better understanding of such applications. Unfortunately, these processes are strongly nonlinear and proven to be very complex to understand with existing tools. In addition, gas temperature increases dramatically behind strong shocks so that real gas effects become important, which includes internal energy excitations, translation-vibration energy relaxation, and chemical reactions among different species.

It is well known that thermal properties of air strongly depend on the temperature [1]. At temperatures less than 500-800K, air flow stays calorically perfect. Only translational and

* Research Associate, AIAA Senior Member, E-mail: xiaowen@seas.ucla.edu
# Professor, AIAA Associate Fellow

rotational energy modes are fully excited whereas the excitation of vibration energy mode and chemical reaction are negligible. At temperatures around 800-2000K, vibration energy mode takes an important role in sharing the total energy with the translational and rotational modes. Near the lower temperature limit of this regime, translation-vibration energy relaxation between harmonic oscillator molecules dominates because most of the molecules are near the ground vibrational state. Although the vibrational oscillation becomes inharmonic as the temperature approaches the dissociation level, results within the harmonic oscillator approximation are known to be sufficiently accurate for most practical purposes [1]. For temperatures above 2000-2500K, vibration energy mode is fully excited and O2 starts dissociating. Around 4000K, O2 is completely dissociated and N2 starts dissociating. When the temperature reaches 9000k, most of the N2 is dissociated. Coincidentally, this is the temperature at which both dissociated N and O atoms start ionized [2].

1. 1 Motivation

A schematic of strong shock and turbulence interaction problem is shown in Fig. 1. In such flows, the coupling between the shock wave and turbulent flow is very strong. Complex linear and nonlinear mechanisms are involved which alter the dynamics of the shock motion and can cause considerable changes in the structure of turbulence and its statistical properties.

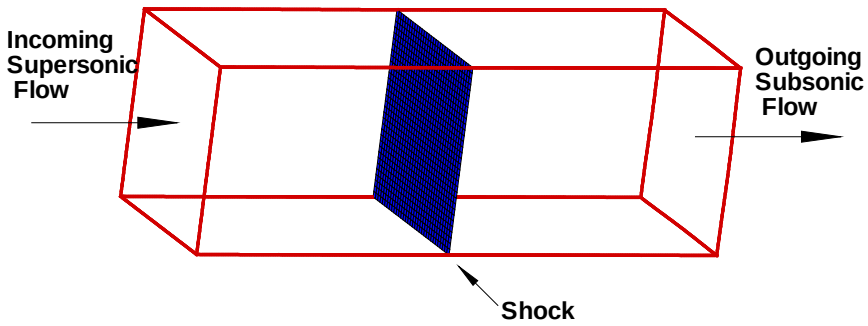

Fig. 1. A schematic of typical setting of strong shock and turbulence interaction [3].

Numerical simulations for such problems have been very limited due to requirements of large computational resources as well as the shortcomings of current numerical methods. The solution of such complex problems warrants very high-order numerical methods. However, popular shock-capturing schemes are not very accurate in this regard as they inherently use numerical dissipation in the whole computational domain. Moreover, spurious numerical oscillations have also been observed when solving strong shock and turbulence interaction problems with shock-capturing schemes [4]. In the past years, interest in various types of vehicles in hypersonic flow regime produced numerous structured grid based nonequilibrium flow solvers. According to recent publications, Laura, DPLR, and US3D are the most frequently referenced and are intensively validated against each other [5]. These codes are efficient in solving nonequilibrium flows. However, they are generally second- and third-order solvers, which may not be good

enough for accurate simulation of shock and turbulence interactions. To avoid such problems, we propose a unique approach of using a high-order shock-fitting and shock-capturing method. The main shock is treated by the shock-fitting method as a sharp boundary of the computational domain. The weak or secondary shocks behind the main shock induced by interactions of the main shock and turbulence are captured by high-order shock-capturing methods. The shock dynamics is governed by a combination of shock jump conditions and a comparability relation from the flow behind main shock. In this way, the interaction of the main shock with freestream turbulence is computed accurately. Compared to shock-capturing methods, the main advantage of the shock-fitting method is uniform high-order accuracy for flow containing shock waves and no spurious oscillations [6]. On the contrary, most of the popular shock-capturing methods are only first-order accurate at the shock and may incur spurious numerical oscillations near the shock.

1.2 Background

Theoretical studies in the field of shock and turbulence interaction have been attempted mostly through linear interaction analysis (LIA) where small perturbations in flow are considered. Kovasznay [7] showed that for weak fluctuations of density, pressure, and entropy, the turbulent fluctuations about mean uniform flow can be decomposed into the vorticity, acoustic, and entropy modes. It was shown that at first-order approximation, each of these modes evolves independently in the inviscid limit. Modifications of random small fluctuations of pressure, entropy and vorticity after passing through shock or flame were studied by Moore [8] and Kerrebrock [9]. It was found that all modes of disturbances are generated in the downstream flow if any of the modes is presented in the upstream flow. More recent theoretical studies of shock and turbulence interaction were carried out by Goldstein [10], Lee et al. [11, 12], Mahesh et al. [13, 14] and Fabre et al. [15]. It was found in these studies that root mean square values of the fluctuating pressure, temperature and density as well as different components of the turbulent kinetic energy are amplified across the shocks.

Since theoretical studies are valid only for very small perturbations, various attempts had been made towards DNS of shock and turbulence interactions since the early 80s. Initial efforts in this area were focused on the interaction of shock with simple disturbance waves. In 1981, Pao and Salas [16] fitted the shock at inflow boundary and solved Euler equation with finite difference discretization to study a shock/vortex interaction. Shock fitting computations with pseudo-spectral (Zang et. al [17]) and spectral techniques (Hussaini et al [18, 19]) were later used to treat the problems in which a single vortex, a vortex sheet, an entropy spot or acoustic wave interacts with the shock. The results obtained from these numerical efforts confirmed the linear theory in the regime of weak shocks. With the advent of essentially non-oscillatory (ENO) and related schemes, a number of shock capturing schemes for compressible flows have been tested for interaction of shock with small disturbances. Although limited to low Mach numbers, these studies mostly confirm the LIA results [19-21].
For studies of a fully turbulent field interacting with shocks, DNS methods and large eddy simulations (LES) have been used. However these different types of methods give

different results when interaction with shock is considered [22]. Most of the recent DNS studies have been on various aspects of interaction of a normal shock with freestream turbulence for relatively weak shock at small Mach numbers. For example, Mahesh et al. [13, 14] did extensive DNS studies of the interaction of a normal shock with an isotropic turbulence. The mean shock Mach numbers were in the range of 1.29 to 1.8. They found that the upstream correlation between the vorticity and entropy fluctuations has strong influence on the evolution of the turbulence across the shock. Lee et al. [12] investigated the effect of Mach numbers on isotropic turbulence interacting with a shock wave. The range of Mach numbers was from 1.5 to 3.0. A shock-capturing scheme was developed to accurately simulate the unsteady interaction of turbulence with shock waves. It was found that turbulence kinetic energy is amplified across the shock wave, and this amplification tends to saturate beyond Mach 3. Hannapel et al. [23] computed shock and turbulence interaction of a Mach 2 shock with a third-order shock-capturing scheme based on the essentially non-oscillatory (ENO) algorithm. Jamme et al. [24] carried out a DNS study of the interaction between normal shock waves of moderate strength (Mach 1.2 and Mach 1.5) and isotropic turbulence. Adams and Shariff [25, 26] proposed a class of upwind-biased finite-difference schemes with a compact stencil for shock and turbulence interaction simulation. They used the non-conservative upwind scheme in smooth region while a shock-capturing ENO scheme was turned on around discontinuities. This idea of hybrid formulation was improved by Pirozzoli [27] who used similar hybrid formulation for a compact weighted essentially non-oscillatory (WENO) scheme with conservative formulation for simulation of shock and turbulence interaction. Ducros et al. [28] conducted LES studies on shock and turbulence interaction by using a second-order finite volume scheme. The method was then used to simulate the interaction of a Mach 1.2 shock with homogeneous turbulence.

According to the brief review, DNS results are currently available for $\mathrm{Re}_\lambda = 12 - 22$, where Re_λ is Reynolds number based Taylor microscale λ. However, the typical Reynolds number in real shock and turbulence interaction experiments are $\mathrm{Re}_\lambda = 200 - 750$ [29]. The highest Reynolds number of flow that can be resolved using DNS is bounded by the available computational resources. It was estimated that for DNS of shock and turbulence interaction with $\mathrm{Re}_\lambda \approx 100$ around 19×10^9 grid points were needed [30]. Prohibitively large computational resources are needed for better understanding of realistic flow situations and inadequate computational resources have been one of the main limitations in past studies. It is also noticed that flows with stronger than Mach 3 shocks have not been considered in the past for shock and turbulence interaction problems. Most of the works in the past used shock-capturing schemes. One of the main issues with shock-capturing schemes is the spurious numerical oscillations created around the shock and the loss of accuracy with dissipation needed to suppress these oscillations especially when strong shocks are encountered [4, 31, 32]. Moreover in shock-capturing schemes the shock spreads over a few grid points. With strong shocks, the thickness of the shock front decreases requiring more resolution for shock-capturing schemes. Thus, lack of adequate computational resources as well as constraints due to choice of algorithms has been another limitation in past studies.

Recently, Rawat and Zhong [3, 33] conducted a series of DNS studies on strong shock and turbulence interactions, with the main focus on high shock Mach number cases. The range of shock Mach number is $M = 2 - 20$. Their results agreed well with those from linear theory and other numerical efforts for weaker than Mach 8 shocks. However, as they increased the shock strengths to the values beyond those considered in the past, new trends were observed. Specifically, it was found that the mean value of streamwise velocity in turbulent postshock flow is larger than corresponding laminar values whereas the mean value of pressure in turbulent postshock flow is smaller than corresponding laminar values (Fig. 2). The difference between turbulent and laminar postshock values decreases as shock strength is increased.

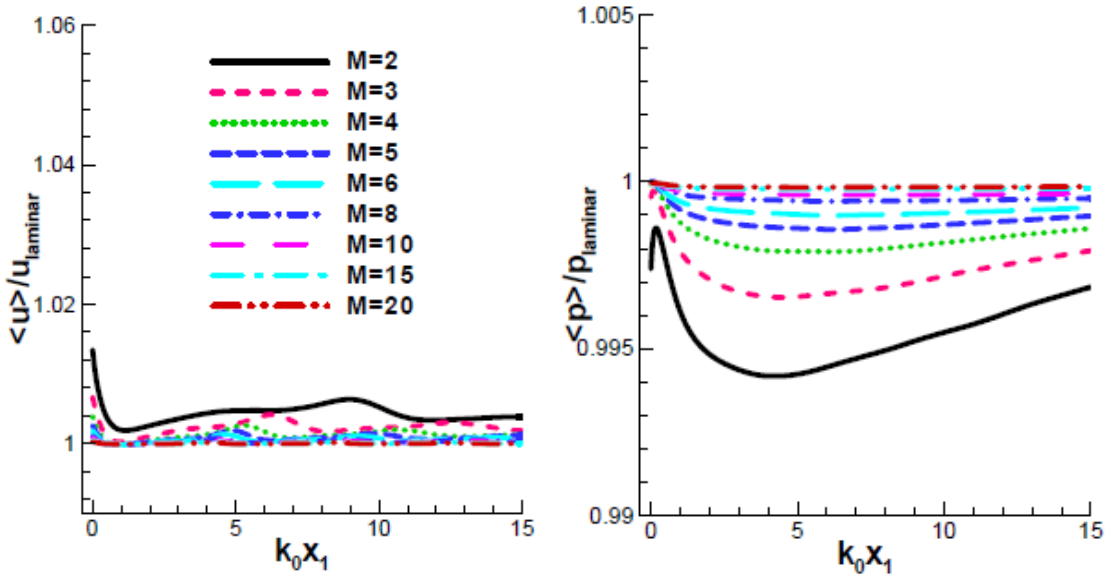

(a) streamwise velocity *(b) pressure*

Fig. 2. Comparison of mean values of flow variables in turbulent postshock flow with the corresponding laminar values[33].

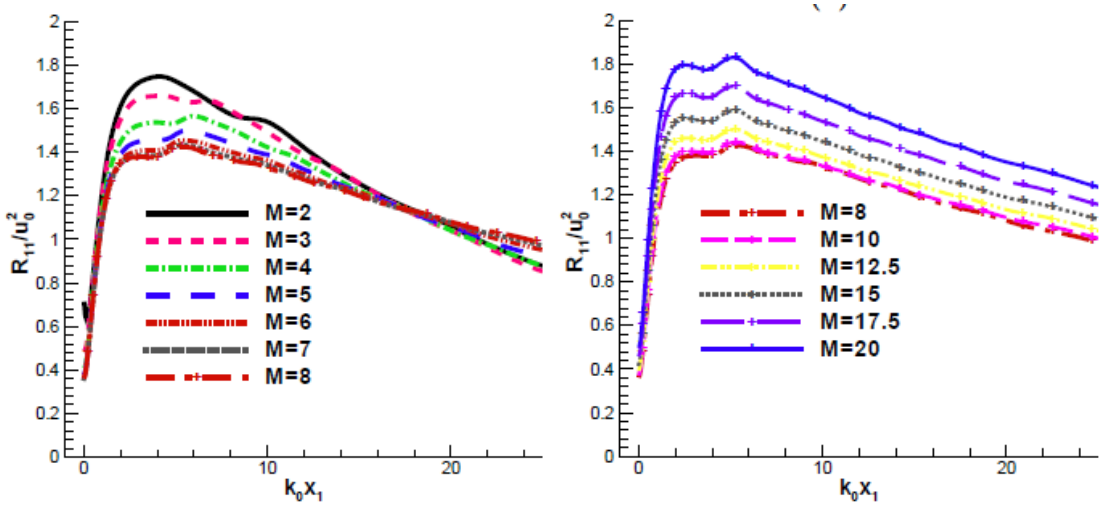

(a) M = 2-8 *(b) M = 8 - 20*

Fig. 3. The amplification in streamwise velocity fluctuations at different shock Mach number [33]

Figure 3 shows the amplification in streamwise velocity fluctuations for cases with different shock Mach number. It was observed to decrease for weaker than Mach 8 shocks, which is in accordance with the linear theory results. This trend, however, reverses for stronger shocks. Same trends were observed for turbulent kinetic energy. Their calculations also showed that, contrary to the previous findings for weaker shocks, increasing shock strength does not simply increase the streamwise vorticity fluctuations. In fact, beyond a certain Mach number, amplification in streamwise vorticity fluctuations decreases and the flow's return to isotropy is delayed (Fig. 4).

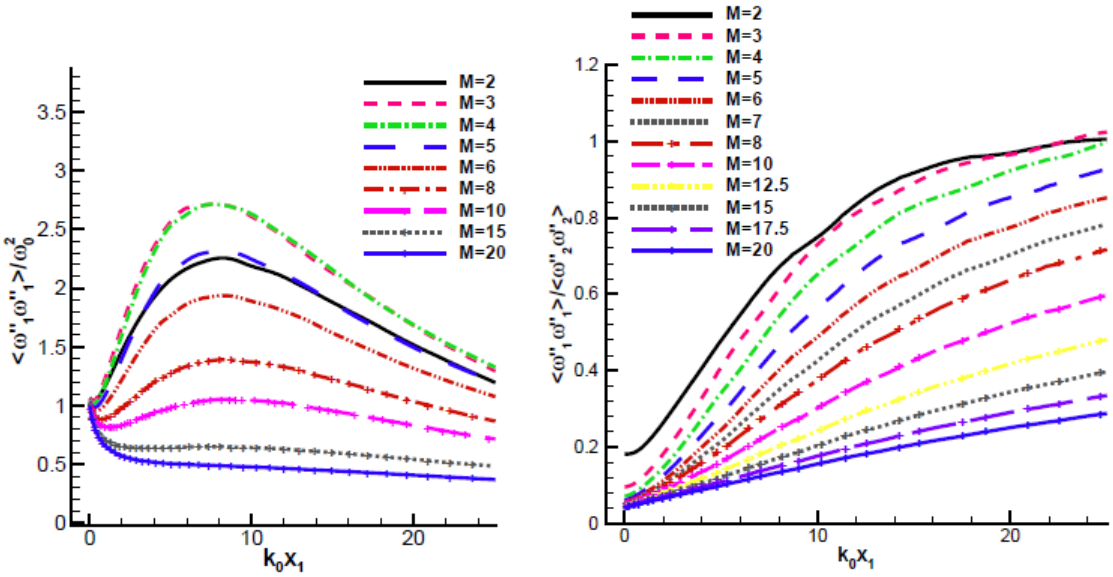

(a) vorticity flucuation *(b) variation of anisotropy*

Fig. 4. Streamwise vorticity fluctuations values for inflow of Re_λ = 29:2 and Mt = 0.124 [33]

The above results are quite exciting. Basically, for very strong shock, new trends of turbulence statistics appear which is never observed in previous researches for weak shocks. But for very strong shocks, it is expected that the real gas effects become quite important, which have not been taken into account in Rawat and Zhong's work.

1.3 Objectives

A study of the literature in the field of shock interactions with turbulence shows that these complex configurations are part of a number of important applications but the current scientific understanding of strong shock turbulence interactions in complex configurations and the ability to reliably predict these strongly nonlinear flows remains limited. We want to carry out DNS studies on large scale computations of strong shock and turbulence interactions, including the real gas effects. The overall objective of this effort is to validate our new 3-D high-order shock-fitting code for nonequilibrium flow simulations and conduct DNS studies on strong shock and turbulence interactions. DNS results will be used to produce a set of highly resolved databases which will be used to develop turbulence models for engineering applications.

The current shock-fitting code is implemented based on a two-temperature model. It is assumed that translational and rotational energy modes are in equilibrium at the translational temperature whereas vibration energy and electronic energy are in equilibrium at the vibration temperature. The flow solver uses the fifth-order shock-fitting method of Zhong [34] with local Lax-Friedrichs flux splitting. The main shock is treated as a sharp boundary of the computational domain. The rest of weak or secondary shocks induced by interactions of the main shock and freestream turbulence are captured by shock-capturing methods. In this paper, a high-order shock-fitting non-equilibrium flow solver based on 5-species air chemistry and recently thermo-chemical models are implemented and tested where the ionizations of N and O are currently not considered. The test of the 11-species air chemistry is ongoing. The solver is being applied to simulate a shock and turbulence interaction problem with shock Mach number being 20.

2. Governing equations and numerical methods

2.1 Governing equation

For nonequilibrium and chemically reactive flows, the governing equations for 5-species air are Navier-Stokes equation with source terms (no radiation). Specifically, they consist of the flowing equations.

$$\frac{\partial \rho_s}{\partial t}+\frac{\partial}{\partial x_j}(\rho_s u_j)-\frac{\partial}{\partial x_j}(\rho D_s \frac{\partial y_s}{\partial x_j})=\omega_s \tag{1}$$

$$\frac{\partial}{\partial t}(\rho u_i)+\frac{\partial}{\partial x_j}(\rho u_i u_j+p\delta_{ij})-\frac{\partial}{\partial x_j}\left[\mu\left(\frac{\partial u_i}{\partial x_j}+\frac{\partial u_j}{\partial x_i}\right)-\frac{2}{3}\mu\frac{\partial u_k}{\partial x_k}\delta_{ij}\right]=0 \tag{2}$$

$$\begin{aligned}\frac{\partial \rho E}{\partial t}+\frac{\partial}{\partial x_j}(\rho H u_j)-\frac{\partial}{\partial x_j}\left[u_i\mu\left(\frac{\partial u_i}{\partial x_j}+\frac{\partial u_j}{\partial x_i}\right)-\frac{2}{3}u_i\mu\frac{\partial u_k}{\partial x_k}\delta_{ij}\right]\\ -\frac{\partial}{\partial x_j}\left(\rho\sum_{s=1}^{5}h_s D_s\frac{\partial y_s}{\partial x_j}\right)-\frac{\partial}{\partial x_j}\left(K\frac{\partial T}{\partial x_j}+K_V\frac{\partial T_V}{\partial x_j}\right)=0\end{aligned} \tag{3}$$

$$\frac{\partial \rho e_V}{\partial t}+\frac{\partial}{\partial x_j}(\rho e_V u_j)-\frac{\partial}{\partial x_j}(\rho\sum_{s=1}^{5}e_{V,s}D_s\frac{\partial y_s}{\partial x_j})-\frac{\partial}{\partial x_j}\left(K_V\frac{\partial T_V}{\partial x_j}\right)=\sum_{s=1}^{3}Q_{T-V,s}+\sum_{s=1}^{5}\omega_s e_{V,s} \tag{4}$$

where,

$$\rho=\sum_{s=1}^{5}\rho_s \qquad y_s=\frac{(c_s/M_s)}{\sum_{i=1}^{5}(c_i/M_i)}$$

$$p=\sum_{s=1}^{5}p_s \qquad p_s=\frac{\rho_s\bar{R}T}{M_s}$$

$$E=\frac{u_i u_i}{2}+\sum_{s=1}^{5}\frac{\rho_s e_s}{\rho} \qquad H=E+\frac{p}{\rho}$$

$\bar{R}$ is the universal gas constant.

The corresponding matrix form of governing equations is as follows,

$$\frac{\partial U}{\partial t}+\frac{\partial F_1}{\partial x}+\frac{\partial F_2}{\partial y}+\frac{\partial F_3}{\partial z}+\frac{\partial G_1}{\partial x}+\frac{\partial G_2}{\partial y}+\frac{\partial G_3}{\partial z}=S \tag{5}$$

Where F stands for inviscid flux,
G stands for viscous flux,
S stands for source terms.

$$U=\left(\rho_1,\rho_2,\ldots,\rho_{11},\rho u,\rho v,\rho w,\rho E,\rho e_V\right)^{\mathrm{T}}$$

The corresponding inviscid and viscous fluxes are

$$F_j=\begin{pmatrix}\rho_1 u_j\\ \rho_2 u_j\\ \vdots\\ \rho_s u_j\\ \rho u u_j+p\delta_{1j}\\ \rho v u_j+p\delta_{2j}\\ \rho w u_j+p\delta_{3j}\\ \rho H u_j\\ \rho e_V u_j\end{pmatrix} \qquad G_j=\begin{pmatrix}\rho_1 v_{1j}\\ \rho_2 v_{2j}\\ \vdots\\ \rho_{11} v_{11j}\\ -\tau_{1j}\\ -\tau_{2j}\\ -\tau_{3j}\\ -u_i\tau_{ij}+q_j+q_{Vj}+\sum_{s=1}^{11}\rho_s h_s v_{sj}\\ q_{Vj}+\sum_{s=1}^{5}\rho_s e_{V,s} v_{sj}\end{pmatrix}$$

Source term is as follows,

$$S=\begin{pmatrix}\omega_1\\ \omega_2\\ \vdots\\ \omega_{11}\\ 0\\ 0\\ 0\\ 0\\ \sum_{s=1}^{3}(Q_{T-V,s}+\omega_s e_{V,s})\end{pmatrix}$$

In above equations, $v_{sj}=u_{sj}-u_j$ is diffusion velocity of species s.

2.2 Coordinate transform

The flow solver uses structured grids. Therefore, the following grid transform is applied.

$$\begin{cases} x = x(\xi,\eta,\zeta,\tau) \\ y = y(\xi,\eta,\zeta,\tau) \\ z = z(\xi,\eta,\zeta,\tau) \\ t = \tau \end{cases} \Leftrightarrow \begin{cases} \xi = \xi(x,y,z,t) \\ \eta = \eta(x,y,z,t) \\ \zeta = \zeta(x,y,z,t) \\ \tau = t \end{cases} \tag{6}$$

Jacobian of the transform,

$$J = \begin{vmatrix} x_\xi & y_\xi & z_\xi & 0 \\ x_\eta & y_\eta & z_\eta & 0 \\ x_\zeta & y_\zeta & z_\zeta & 0 \\ x_\tau & y_\tau & z_\tau & 1 \end{vmatrix} \tag{7}$$

With the transform relation, the governing equations in (ξ,η,ζ,τ) coordinate system are written as

$$\frac{\partial(JU)}{\partial\tau} + \frac{\partial\tilde{F}_1}{\partial\xi} + \frac{\partial\tilde{F}_2}{\partial\eta} + \frac{\partial\tilde{F}_3}{\partial\zeta} + \frac{\partial\tilde{G}_1}{\partial\xi} + \frac{\partial\tilde{G}_2}{\partial\eta} + \frac{\partial\tilde{G}_3}{\partial\zeta} = JS \tag{8}$$

Where

$$\begin{aligned} \tilde{F}_1 &= J\xi_x F_1 + J\xi_y F_2 + J\xi_z F_3 + JU\xi_t \\ \tilde{F}_2 &= J\eta_x F_1 + J\eta_y F_2 + J\eta_z F_3 + JU\eta_t \\ \tilde{F}_3 &= J\zeta_x F_1 + J\zeta_y F_2 + J\zeta_z F_3 + JU\zeta_t \\ \tilde{G}_1 &= J\xi_x G_1 + J\xi_y G_2 + J\xi_z G_3 \\ \tilde{G}_2 &= J\eta_x G_1 + J\eta_y G_2 + J\eta_z G_3 \\ \tilde{G}_3 &= J\zeta_x G_1 + J\zeta_y G_2 + J\zeta_z G_3 \end{aligned}$$

2.3 Numerical method

The governing equations are solved by the fifth-order shock-fitting method of Zhong [34]. For the thermally non-equilibrium and chemically reacting system (5) in the direction, $\mathrm{k} = (k_1, k_2, k_3)$, the corresponding inviscid flux term is

$$\mathrm{F} = \begin{pmatrix} \rho_1 \mathrm{k}\,\mathrm{u} \\ \rho_2 \mathrm{k}\,\mathrm{u} \\ \rho_3 \mathrm{k}\,\mathrm{u} \\ \vdots \\ \rho_{11} \mathrm{k}\,\mathrm{u} \\ \rho u \mathrm{k}\,\mathrm{u} + pk_1 \\ \rho v \mathrm{k}\,\mathrm{u} + pk_2 \\ \rho w \mathrm{k}\,\mathrm{u} + pk_3 \\ \rho H \mathrm{k}\,\mathrm{u} \\ \rho e_V \mathrm{k}\,\mathrm{u} \end{pmatrix} \tag{9}$$

Hence the Jacobian of flux is defined as,

$$\mathrm{A} = \frac{\partial \mathrm{F}}{\partial \mathrm{U}} = L\Lambda R \tag{10}$$

$$A = |\mathrm{k}| \begin{bmatrix} \tilde{U}(\delta_{sr} - c_s) & c_s n_x & c_s n_y & c_s n_z & 0 & 0 \\ \tilde{\gamma}_r n_x - \tilde{U}u & -\beta u n_x + u n_x + \tilde{U} & -\beta v n_x + u n_y & -\beta w n_x + u n_z & \beta n_x & \phi n_x \\ \tilde{\gamma}_r n_y - \tilde{U}v & -\beta u n_y + v n_x & -\beta v n_y + v n_y + \tilde{U} & -\beta w n_y + v n_z & \beta n_y & \phi n_y \\ \tilde{\gamma}_r n_z - \tilde{U}w & -\beta u n_z + w n_x & -\beta v n_z + w n_y & -\beta w n_z + w n_z + \tilde{U} & \beta n_z & \phi n_z \\ \tilde{\gamma}_r \tilde{U} - \tilde{U}H & -\beta u \tilde{U} + H n_x & -\beta v \tilde{U} + H n_y & -\beta w \tilde{U} + H n_z & \beta \tilde{U} + \tilde{U} & \phi \tilde{U} \\ -\tilde{U} e_V & e_V n_x & e_V n_y & e_V n_z & 0 & \tilde{U} \end{bmatrix}$$

$$R = \begin{bmatrix} a^2 \delta_{sr} - c_s \tilde{\gamma}_r & \beta u c_s & \beta v c_s & \beta w c_s & -\beta c_s & -\phi c_s \\ -\tilde{V} & l_x & l_y & l_z & 0 & 0 \\ -\tilde{W} & m_x & m_y & m_z & 0 & 0 \\ \tilde{\gamma}_r - \tilde{U}a & a n_x - \beta u & a n_y - \beta v & a n_z - \beta w & \beta & \phi \\ \tilde{\gamma}_r + \tilde{U}a & -a n_x - \beta u & -a n_y - \beta v & -a n_z - \beta w & \beta & \phi \\ -e_V \tilde{\gamma}_r & \beta u e_V & \beta v e_V & \beta w e_V & -\beta e_V & a^2 - \phi e_V \end{bmatrix}$$

$$L = \begin{bmatrix} \delta_{sr}/a^2 & 0 & 0 & c_s/2a^2 & c_s/2a^2 & 0 \\ u/a^2 & l_x & m_x & (u + a n_x)/2a^2 & (u - a n_x)/2a^2 & 0 \\ v/a^2 & l_y & m_y & (v + a n_y)/2a^2 & (v - a n_y)/2a^2 & 0 \\ w/a^2 & l_z & m_z & (w + a n_z)/2a^2 & (w - a n_z)/2a^2 & 0 \\ \left[\beta(u^2 + v^2 + w^2) - \tilde{\gamma}_r\right]/\beta a^2 & \tilde{V} & \tilde{W} & (H + a\tilde{U})/2a^2 & (H - a\tilde{U})/2a^2 & -\phi/\beta a^2 \\ 0 & 0 & 0 & e_V/2a^2 & e_V/2a^2 & 1/a^2 \end{bmatrix}$$

The eigenvalues of Jacobian matrix (10) are

$$\lambda_{1,2,3,4,5,6,7,10} = |\mathrm{k}|\tilde{U} \tag{11}$$

$$\lambda_8 = |\mathrm{k}|(\tilde{U} + a) \tag{12}$$

$$\lambda_9 = |\mathrm{k}|(\tilde{U} - a) \tag{13}$$

where subscript “s” refers to row s and species s, whereas subscript “r” refers to column r and species r. Both s and r vary from 1 to 5 in the present model. The unit vector n is defined from vector k as

$$\mathrm{n} = (n_x, n_y, n_z) = \frac{(k_1, k_2, k_3)}{|\mathrm{k}|}$$

$\mathrm{l} = (l_x, l_y, l_z)$ and $\mathrm{m} = (m_x, m_y, m_z)$ are two unit vectors such that n , l , and m are mutually orthogonal.

$$\tilde{U} = un_x + vn_y + wn_z$$
$$\tilde{V} = ul_x + vl_y + wl_z$$
$$\tilde{W} = um_x + vm_y + wm_z$$

The derivative of pressure respecting to conservative variables comes from

$$dp = \beta(d\rho E - ud\rho u - vd\rho v - wd\rho w) + \phi d\rho e_V + \tilde{\gamma}_s d\rho_s \tag{14}$$

Where

$$\beta = \frac{\bar{R}}{\rho \sum_s c_s c_{v,tr}^s} \sum_{r=1}^{10} \frac{\rho_r}{M_r} \tag{15}$$

$$\phi = \frac{\bar{R}}{\rho C_{v,V}} \frac{\rho_e}{M_e} - \beta \tag{16}$$

$$\tilde{\gamma}_s = \frac{\bar{R} T_q}{M_s} + \beta \frac{u^2 + v^2 + w^2}{2} - \beta e_s - \phi e_{V,s} \tag{17}$$

$$a^2 = \sum_{s=1}^{11} c_s \tilde{\gamma}_s + \beta \left[H - (u^2 + v^2 + w^2) \right] + \phi e_V = (1 + \beta) \frac{p}{\rho} \tag{18}$$

In equation (17), $T_q = T_V$ when s is an electron, otherwise, $T_q = T$.

The main computational method we will use for this study is a fifth-order shock fitting code [34]. The flow variables behind the shock are determined by Rankine-Hugoniot relations across the main shock and a characteristic compatibility relation from behind the shock. With the assumptions of "frozen" flow (on chemical reactions and energy relaxations when flow passes through the shock), the species mass fractions and vibration temperature keep constant on the two sides of the shock where translation temperature jumps across the shock. In this way, shock jumps conditions for total density, momentum and total energy are the same as those for perfect gas. In addition, the compatibility relation relating to the maximum eigenvalue in wall normal direction is used.

In shock-fitting method, the velocity and location of the shock are solved as part of the solutions. In the interior, compressible Navier-Stokes equations are solved in fully conservative form. Discretization of governing equation is carried out using fifth-order finite difference schemes for spatial terms and explicit Runge-Kutta (generally RK-3) schemes. For sufficiently smooth flow behind the shock, we mostly use fifth-order upwind scheme of Zhong [34] for discretization of spatial terms. However, for shock and turbulence interaction problems, sufficiently high turbulence intensities might produce secondary shocks behind the main shock. To handle such cases, shock-capturing methods are used to solve the flow behind the main shock. All our methods are coded based on message passing interface (MPI) is used for communication in the parallel computations.

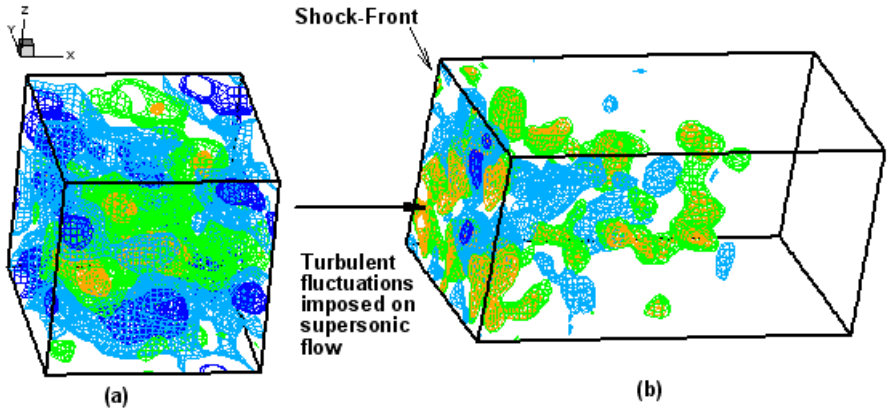

Fig. 5. Schematic showing typical density contours and computational domains for simulation of shock-turbulence interaction using shock-fitting algorithm [3].

With the shock-fitting algorithm for the problem shown in Fig. 1, there is no need to solve the supersonic flow upstream of the shock. Hence, computational domain for the shock-fitting method for shock and turbulence interaction consists of flow only downstream of the shock. The supersonic turbulent flow ahead of the shock can be computed in a separate simulation. A schematic of the shock-fitting implementation for the shock-turbulence interaction problem is shown in Fig. 5. The inflow turbulence is generated using a separate direct numerical simulation as shown in Fig. 5(a). We compute decaying isotropic turbulence in a periodic box to generate the realistic turbulent fluctuations that can be used as incoming turbulence for the shock-fitting algorithm. The computational domain for implementation of shock-fitting algorithm is shown in Fig. 5(b). The shock front forms the left boundary of the computational domain.

The turbulent fluctuations generated from Fig. 5(a) are imposed on supersonic flow and used as inflow condition at the shock following the Taylor's hypothesis that is valid for small turbulent intensities ($M_t < 0.5$ and $u'_{1rms} / \bar{u}_1 < 0.15$) [35]. For higher turbulent intensities, it is advisable to carry out simulation of spatially decaying turbulence which is more expensive. From the temporal simulations inside a periodic box, we obtain values of flow variables at fixed grid points of the box while due to shock-movement grid points in shock-fitting computations are not stationary. Moreover, when the turbulent box is convected through the shock in the shock-fitting computations, the shock-points generally do not align with grid points of the turbulent box. Hence, values on the supersonic side of the shock are computed using interpolations. Since in our shock-fitting formulation the grids move in only one direction (X-direction in Fig. 5(b)), one dimensional Fourier interpolation is sufficient for this purpose. As a boundary condition, shock-fitting formulation needs the values of the time derivatives of conservative variables ahead of the shock according to the isotropic field which using Taylor's hypothesis are taken as appropriate spatial derivatives. Together with one characteristic coming to the shock from the high pressure side, these values determine the time derivatives at the downstream side. Thus, they are calculated from the corresponding upstream values, using the Rankine–Hugoniot conditions. Periodic boundary conditions are used in the transverse directions and non-reflecting characteristic boundary conditions are used at the subsonic exit of the computational domain.

3. Nonequilibrium models

3.1 Model of vibration and electron energy

To consider the high temperature effects, the model of vibration and electron energy used in Hash et al.'s paper [5] are implemented in the code. Vibration energy and electron energy are considered separately with different formula. Specific total enthalpy of species and specific heat in constant pressure of species are defined as,

$$h_s = c_{vs}T + \frac{p_s}{\rho_s} + E_V + h_s^0 \tag{19}$$

$$c_p^s = c_v^s + \frac{\bar{R}}{M_s} + c_V^s \tag{20}$$

where h_s^0 is the generation enthalpy of species. The variables on the right hand side of equations (19) and (20) are calculated from the following formula,

$$E_V = (e_v + e_{els}) = \frac{\bar{R}}{M_s}\left(\sum_{s=1}^{3} \frac{\theta_{vs}}{e^{\theta_{vs}/T_V} - 1} + \sum_{s=1}^{5} \frac{\sum_{i=1}^{\infty} g_{i,s}\theta_{el,i,s} \exp(-\theta_{el,i,s}/T_V)}{\sum_{i=0}^{\infty} g_{i,s} \exp(-\theta_{el,i,s}/T_V)} \right)$$

$$c_v^s = c_{vtr,s} + c_{vrot,s} \quad c_{vtr,s} = \frac{3\bar{R}}{2M_s} \qquad c_{vrot,s} = \begin{cases} \dfrac{\bar{R}}{M_s} & (s = 1,3) \\ 0 & (otherwise) \end{cases}$$

$$c_V^s = \frac{\bar{R}}{M_s}\left\{ \frac{(\theta_{vs}/T_V)^2 e^{\theta_{vs}/T_V}}{\left(e^{\theta_{vs}/T_V} - 1\right)^2} + \frac{\left[\sum_{i=1}^{\infty} g_{i,s}\left(\theta_{el,i,s}/T_V\right)^2 \exp(-\theta_{el,i,s}/T_V)\right]}{\sum_{i=0}^{\infty} g_{i,s} \exp(-\theta_{el,i,s}/T_V)} \right.$$

$$\left. - \frac{\left[\sum_{i=1}^{\infty} g_{i,s}\theta_{el,i,s} \exp(-\theta_{el,i,s}/T_V)\right]\left[\sum_{i=0}^{\infty} g_{i,s}\left(\theta_{el,i,s}/T_V^2\right) \exp(-\theta_{el,i,s}/T_V)\right]}{\left(\sum_{i=0}^{\infty} g_{i,s} \exp(-\theta_{el,i,s}/T_V)\right)^2} \right\}$$

The related parameters are listed in Table 1 and Table 2.

Table 1. Parameters used vibration energy model

Species	h_s^0 (J/kg)	M_s (g)	θ_{vs} (K)
N2	0	28	3395
O2	0	32	2239
NO	2.996123e6	30	2817
N	3.362161e7	14	-
O	1.543119e7	16	-

Table 2. Electronic energy states for 5-species air

Species	Θ (K)	g	Species	Θ (K)	g	Species	ΘO (K)	g
N2	0	1	O2	1.13916e4	2	NO	8.88608e4	4
N2	7.22316e4	3	O2	1.89847e4	1	NO	8.98176e4	4
N2	8.57786e4	6	O2	4.75597e4	1	NO	8.98845e4	2
N2	8.60503e4	6	O2	4.99124e4	6	NO	9.04270e4	2
N2	9.53512e4	3	O2	5.09227e4	3	NO	9.06428e4	2
N2	9.80564e4	1	O2	7.18986e4	3	NO	9.11176e4	4
N2	9.96827e4	2	NO	0	4	N	0	4
N2	1.04898e5	2	NO	5.46735e4	8	N	2.76647e4	10
N2	1.11649e5	5	NO	6.31714e4	2	N	4.14931e4	6
N2	1.22584e5	1	NO	6.59945e4	4	O	0	5
N2	1.24886e5	6	NO	6.90612e4	4	O	2.27708e2	3
N2	1.28248e5	6	NO	7.0500e4	4	O	3.26569e2	1
N2	1.33806e5	10	NO	7.49106e4	4	O	2.28303e4	5
N2	1.40430e5	6	NO	7.62888e4	2	O	4.86199e4	1
N2	1.50496e5	6	NO	8.67619e4	4			
O2	0	3	NO	8.71443e4	2			

3.2 Thermal properties

For the 5-species air, a more complex model of thermal properties is applied [36]. According to this model, thermal properties are calculated as follows,

$$\mu = \sum_s \frac{m_s \gamma_s}{\sum_r \gamma_r \Delta_{sr}^{(2)}(T)} \quad \textbf{(g/cm-sec)} \tag{21}$$

$$K_T = \frac{15}{4} k \sum_s \frac{\gamma_s}{\sum_r a_{sr} \gamma_r \Delta_{sr}^{(2)}(T)} \quad \textbf{(J/cm-sec-K)} \tag{22}$$

In above equation, $a_{sr} = 1 + \dfrac{\left[1-(m_s/m_r)\right]\left[0.45-2.54(m_s/m_r)\right]}{\left[1+(m_s/m_r)\right]^2}$

$$K_R = k \sum_{s=1,2,3} \frac{\gamma_s}{\sum_r \gamma_r \Delta_{sr}^{(1)}(T)} \quad \textbf{(J/cm-sec-K)} \tag{23}$$

$$K_{V-E} = k\frac{C_{V,V}}{R}\sum_{s=1}^{5}\frac{\gamma_s}{\sum_r \gamma_r \Delta_{sr}^{(1)}(T)} \textbf{ (J/cm-sec-K)} \tag{24}$$

To calculate viscosity and heat conductivity, from equation (21) to equation (24), the collision terms are as follows,

$$\Delta_{sr}^{(1)}(T) = \frac{8}{3}\left[\frac{2m_s m_r}{\pi RT(m_s+m_r)}\right]^{1/2} 10^{-20}\pi\Omega_{sr}^{(1,1)}(T) \textbf{ (cm-sec)}$$

$$\Delta_{sr}^{(2)}(T) = \frac{16}{3}\left[\frac{2m_s m_r}{\pi RT(m_s+m_r)}\right]^{1/2} 10^{-20}\pi\Omega_{sr}^{(2,2)}(T) \textbf{ (cm-sec)}$$

Collision integrals involving neutrals (Non-Coulombic collision integrals) are

$$\pi\Omega_{sr}^{(l,j)}(T) = DT^{\left[A(\ln T)^2 + B\ln T + C\right]} \ (\overset{0}{\mathrm{A}}^2) \tag{25}$$

Species diffusion coefficients are defined as,

$$D_s = \frac{(1-y_s)}{\sum_{r\neq s}\left(y_r / D_{sr}\right)} \tag{26}$$

where y_s is the molar fraction. For binary diffusion between heavy particles,

$$D_{sr} = \frac{kT}{p\Delta_{sr}^{(1)}(T)}$$

3.3 Chemical source terms

Five reactions for the five species air,

$$N_2 + M = 2N + M$$
$$O_2 + M = 2O + M$$
$$NO + M = N + O + M$$
$$N_2 + O = NO + N$$
$$NO + O = O_2 + N$$

Reaction rates,

$$R_1 = \sum_m \left[-k_{f_1 m}\frac{\rho_{N_2}}{M_{N_2}}\frac{\rho_m}{M_m} + k_{b_1 m}\frac{\rho_N}{M_N}\frac{\rho_N}{M_N}\frac{\rho_m}{M_m}\right]$$

$$R_2 = \sum_m \left[-k_{f_2 m}\frac{\rho_{O_2}}{M_{O_2}}\frac{\rho_m}{M_m} + k_{b_2 m}\frac{\rho_O}{M_O}\frac{\rho_O}{M_O}\frac{\rho_m}{M_m}\right]$$

$$R_3 = \sum_m \left[-k_{f_3 m} \frac{\rho_{NO}}{M_{NO}} \frac{\rho_m}{M_m} + k_{b_3 m} \frac{\rho_N}{M_N} \frac{\rho_O}{M_O} \frac{\rho_m}{M_m} \right]$$

$$R_4 = -k_{f_4} \frac{\rho_{N_2}}{M_{N_2}} \frac{\rho_O}{M_O} + k_{b_4} \frac{\rho_{NO}}{M_{NO}} \frac{\rho_N}{M_N}$$

$$R_5 = -k_{f_5} \frac{\rho_{NO}}{M_{NO}} \frac{\rho_O}{M_O} + k_{b_5} \frac{\rho_{O_2}}{M_{O_2}} \frac{\rho_N}{M_N}$$

Correspondingly, the source terms are as follows,

$$\begin{cases} \omega_{N_2} = M_{N_2}(R_1 + R_4) \\ \omega_{O_2} = M_{O_2}(R_2 - R_5) \\ \omega_{NO} = M_{NO}(R_3 - R_4 + R_5) \\ \omega_N = M_N(-2R_1 - R_3 - R_4 - R_5) \\ \omega_O = M_O(-2R_2 - R_3 + R_4 + R_5) \end{cases}$$

3.4 Energy relaxation

In two temperature model, energy relaxation only happens between translation energy and vibration & electron energy, which can be expressed as

$$Q_{T-v,s} = \rho_s \frac{e_{vs}^*(T) - e_{vs}}{\tau_{vs}} \tag{27}$$

where, $e_{vs}^*(T)$ is the vibration energy per unit mass of species s evaluated at the local translational temperature.

$$\tau_{vs} = \left\langle \tau_{s,L-T} \right\rangle + \tau_{cs} = \frac{\sum_r y_r}{\sum_r y_r / \tau_{sr,L-T}} + \frac{1}{a_s \sigma_v N_s} \qquad (a_s = \sqrt{\frac{8\bar{R}T}{\pi M_s}})$$

$$\tau_{sr,L-T} = \frac{1}{p} \exp\left[A_{sr} \left(T^{-1/3} - 0.015 \mu_{sr}^{1/4} \right) - 18.42 \right] \text{ (p in atm)}$$

$$A_r = 1.16 \times 10^{-3} \mu_{sr}^{1/2} \theta_{vs}^{4/3} \qquad \mu_{sr} = M_s M_r / (M_s + M_r)$$

$$S_s = 3.5 \exp\left(-\theta_s / T_{shk} \right) \qquad \sigma_v = 10^{-21} \left(50,000 / T \right)^2$$

Here, θ_s is a defined characteristic temperature.

4. Test of shock-fitting method and nonequilibrium models

The two-temperature model of air has been implemented to the fifth-order shock-fitting method with recent models of thermochemical models. Since a number of test cases of

shock and freestream disturbance/turbulence interaction have been evaluated by Rawat and Zhong [3] for the shock-fitting method under perfect gas assumption, we will focus our tests on thermochemical models.

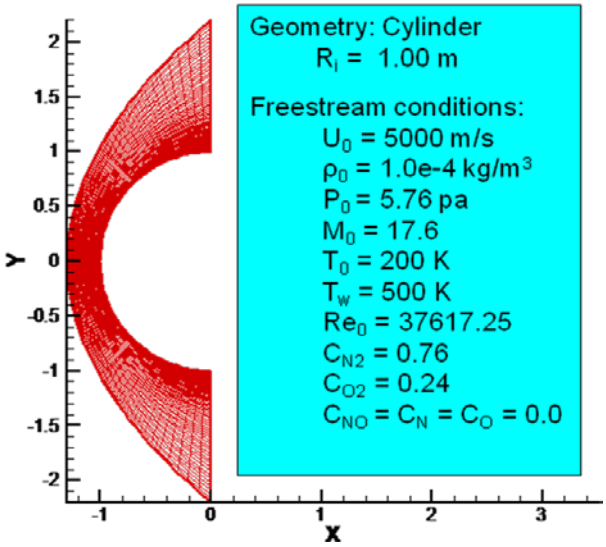

Fig. 6. Mesh sturcture and flow conditions of the test case.

Figure 6 shows the mesh and flow conditions of the test case: 5-species air over a 1-meter radius cylinder. The temperatures on the cylinder are equal to Tw (= 500 K). Catalytic boundary conditions are applied on the wall for species mass fraction. Total density is computed from pressure and translational temperature. Then species densities are calculated with total density and mass fraction. Total energy and vibration energy are calculated using species densities and two temperatures. The mass fractions of initial gas are as follows,

CN2 = 0.76, CO2 = 0.24

CNO = CN = CO = 0

To make the results comparable, flow conditions are exactly the same as what Gnoffo used in his simulation. The simulation results are compared with Gnoffo's results obtained from Laura.

Figure 7 compares flow field contours obtained from current shock-fitting code with those obtained from Laura code. From the contours of pressure, temperatures, and NO density, it is found that shock standoff distances of the two sets of simulations have a good agreement. In addition, the flow fields near the wall have a good agreement. Near the shock, there is small discrepancy between the two sets of solution, mainly due to the different treatment of shock wave. Unlike the shock-fitting code, shock-capturing TVD scheme is applied in Laura code. Figure 7(c) shows that the vibration temperature of shock-fitting solution is significant different from that of Laura in the shock layer, which is mainly caused by the different models of vibration and electronic energy. Laura code used curved fitted vibration and electronic energy [37], whereas we used separate models for vibration energy and electronic energy. Since the shock-fitting code is implemented

for DNS of strong shock and turbulence interaction, the separate models of vibration and electronic energy is preferred, because it can apply to all range of temperature.

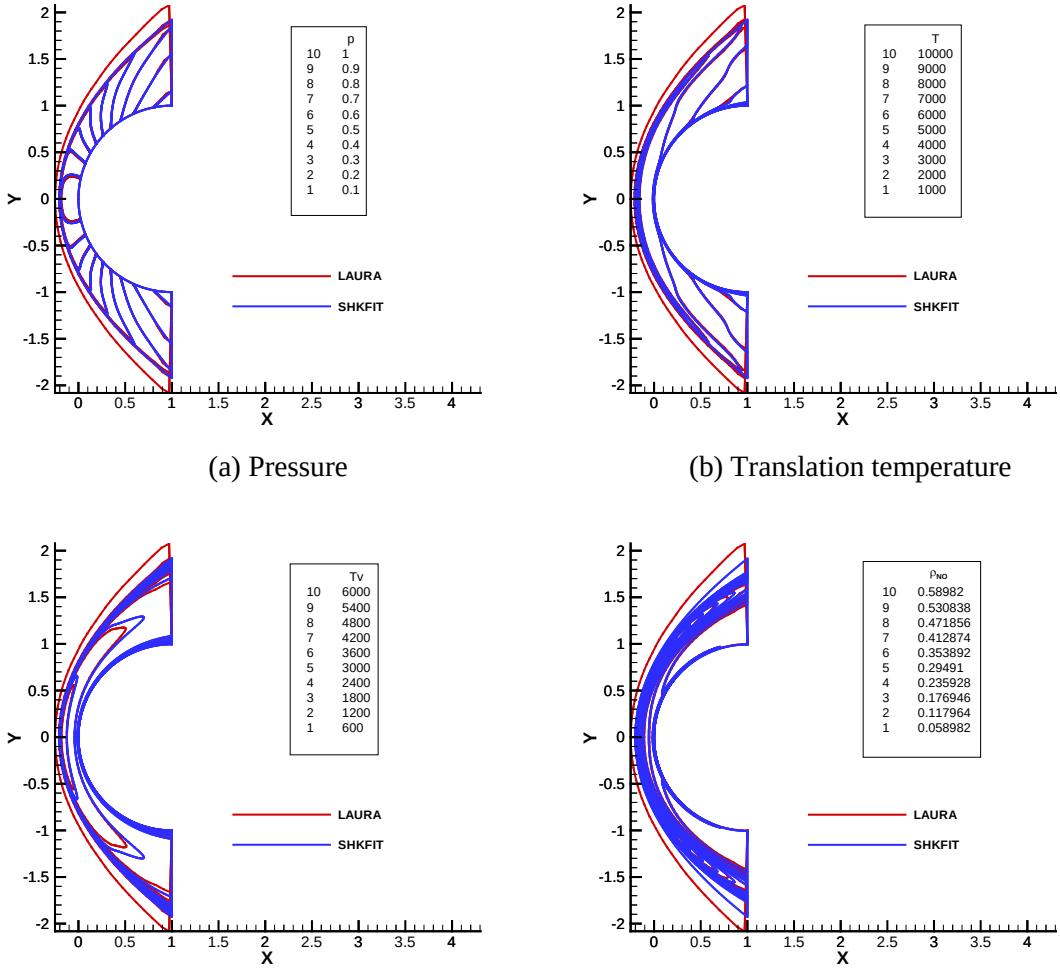

(a) Pressure

(b) Translation temperature

(c) Vibration temperature

(d) Species density of NO

Fig. 7. Comparisons of flow field contours obtained from shock-fitting code with those obtained from Laura simulation.

Since we have detailed flow field information obtained from the Laura code, we can also compare the distributions of flow variables along the stagnation line or along the cylinder surface. For example, figure 8 compares flow variables along the stagnation line obtained from current shock-fitting code with those obtained from Laura code. These two figures also show that shock standoff distances of the two sets of simulations have a good agreement considering the different treatment of the bow shock. The distributions of temperatures and species densities along the stagnation line have a good agreement near the wall and have small discrepancy near the shock. Again, the discrepancy near the shock is due to the different treatment of shock wave. Overall, Figures 7 and 8 indicate that our shock-fitting nonequilibrium flow solver is reliable for the simulation of strong shock and turbulence interaction.

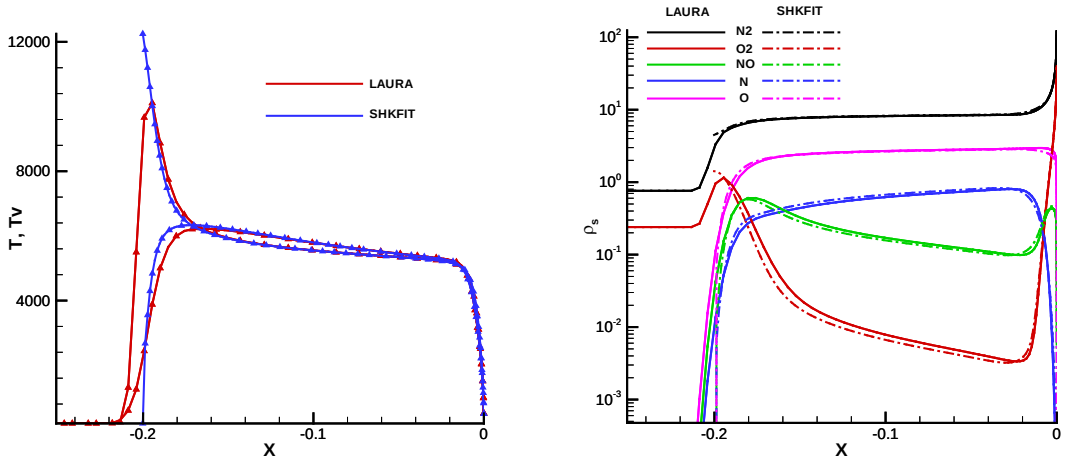

(a) Temperatures (b) Species densities

Fig. 8. Comparisons of flow variables along the stagnation line obtained from shock-fitting code with those obtained from Laura simulation.

5. Strong shock and turbulence interaction

After validating the themo-chemical models of the shock-fitting nonequilibrium solver, we apply the solver to simulate a shock and turbulence interaction problem with shock Mach number being 20. The original plan is to run this case for both perfect gas and real gas, and then compare the two results to inverstigate the real gas effects on shock and turbulence interaction. Due to the tremendous cost of computer resources that the nonequilibrium simulation requests, no numerical result is yet obtained for this problem with real gas effects. Numerical simulation of this problem for real gas is ongoing and more results will be obtained soon. In this section, we reported some results for the inflow simulation.

As domensrated in Fig. 5, we first simulate decaying isotropic turbulence in a periodic box to generate the realistic turbulence. Using the Taylor hypothesis, the turbulence fluctuations generated in the periodic box (Fig. 5(a)) are then imposed to the shock as incoming turbulence for the shock-fitting solver. In the computation domain shown in Fig. 5(b), periodic boundary conditions are used in the transverse directions and non-reflecting characteristic boundary conditions are used at the subsonic exit of the computation domain. The procedure to generate inflow turbulence is the same as that of Erlebacher [38]. The main steps of this method are as follows,

1. As initial conditions for the inflow computations, a field of random fluctations is generated, including velocity, density, and temperature variables.
2. Initial velocity fluctuations are decomposed into solenoidal ($\nabla \cdot \mathrm{V} = 0$) and dilatational components ($\nabla \times \mathrm{V} = 0$). For the decomposition, Fourier transform of velocity fluctuations are obtained ($\hat{u}_i$, $i = 1, 2, 3$), then

$$\hat{u}_i^{\mathcal{S}} = u_i - k_i (k_j u_j / k^2) \tag{28}$$

$$\hat{u}_i^{\mathcal{D}} = u_i - u_i^S \tag{29}$$

3. Impose a prescribed spectra to the solenoidal velocity fluctuations,

$$E(k)=\frac{16}{k_0}\sqrt{\frac{2}{\pi}}\left(\frac{k}{k_0}\right)^4\left(u_{rms}^0\right)^2\exp\left[-2\left(k/k_0\right)^2\right] \tag{30}$$

where k_0 is the most energetic wave number and u_{rms}^0 is the root mean square of velocity fluctuations. This definition of energy density spectra ensures the total fluctuation energy relation,

$$\int_0^\infty E(k)dk=\frac{3}{2}\left(u_{rms}^0\right)^2 \tag{31}$$

4. The flow variables are transformed to the physical space and scaled to have desired root mean square fluctuations.
5. A temporal decaying isotropic turbulence is computed in a periodic box using the fluctuations as initial conditions. According to literature [12, 39], the turbulence is considered realistic when the skewness of streamwise velocity derivative reaches a steady value between -0.4 and -0.6. The skewness of velocity derivative is defined as

$$S_1=\overline{\left(\partial u_1/\partial x_1\right)^3}\Big/\overline{\left[\left(\partial u_1/\partial x_1\right)^2\right]}^{3/2} \tag{32}$$

In current simulation, the parameters of inflow simulations are set as follows,

$k_0=2$ $\qquad$ $u_{rms}^0=1$

$\overline{\rho_1}=0$ $\qquad$ $\overline{T_1}=0$

$M_{t,0}=0.4$ $\qquad$ $\lambda_0=k_0/2$

$\mathrm{Re}_{\lambda,0}=50$ $\qquad$ $\mu_0=\overline{\rho_1}u_{rms}^0\lambda_0/\mathrm{Re}_{\lambda,0}$

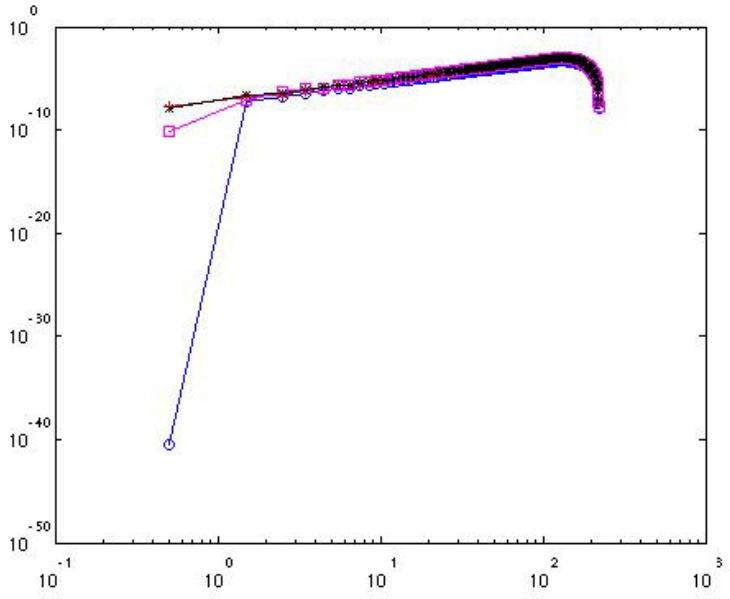

Fig. 9. Spectra of random fluctuations of flow variables (step 1).

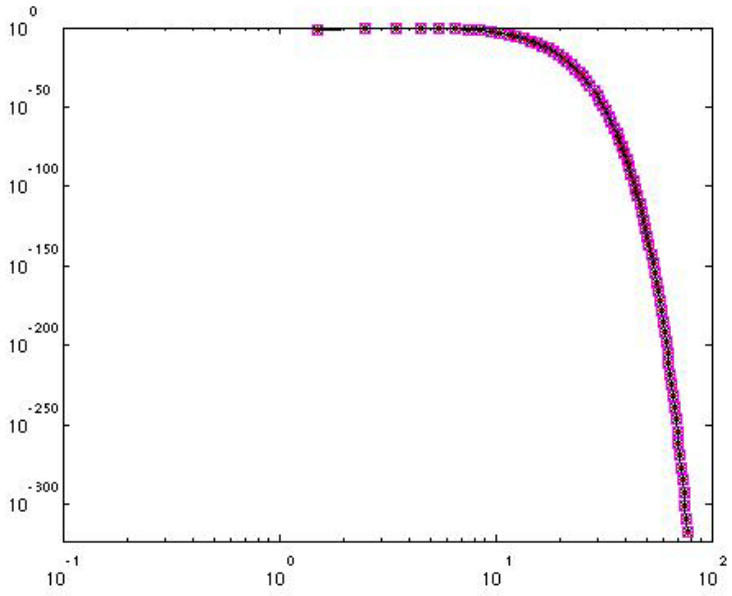

Fig. 10. Spectra of scaled fluctuations of flow variables (step 4).

Figures 9 and 10 show the energy spectra of fluctuations of flow variables before and after imposing the prescribed spectra. The fluctuation shown in Fig. 10 is used as initial conditions for the inflow simulation. Figure 11 shows the development of skewness for the inflow simulation. It shows that, as time evolves, turbulence statistics evolve rapidly and reach to a steady level around $t = 0.7\lambda_0 / u^0_{rms}$. After reaching to the steady state, the turbulence fluctuations at any time can be used as freestream turbulence for the shock-fitting simulations. Figure 12 shows that the Reynolds number based on Taylor lengthscale keeps decaying.

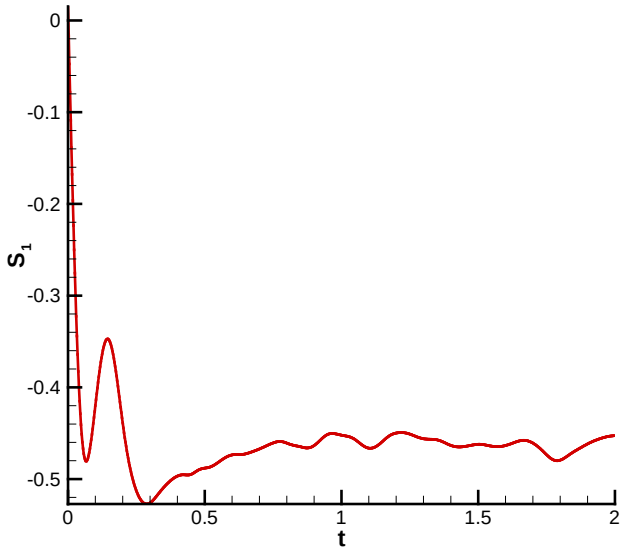

Fig. 11. Temporal development of skewness for the inflow simulation.

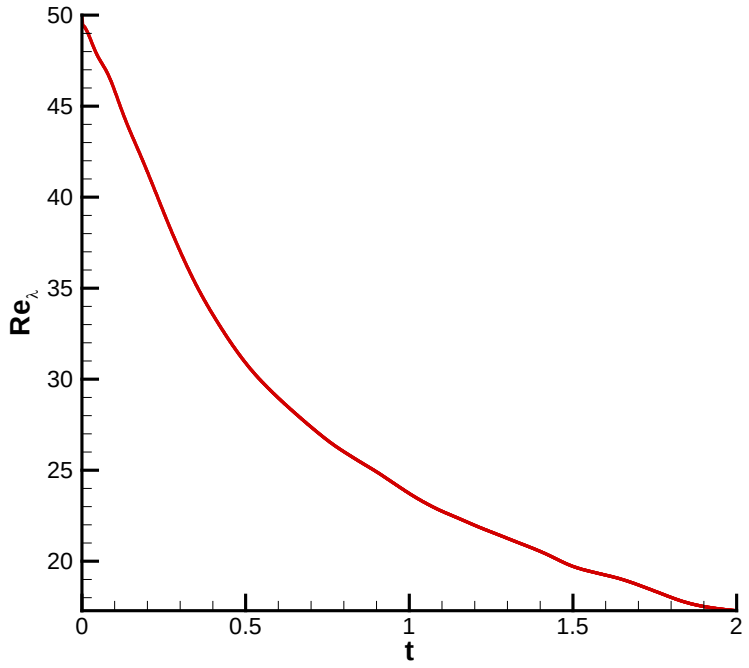

Fig. 12. Temporal development of Reynolds number for the inflow simulation.

6. Summary and Future Plan

In current paper, a high-order shock-fitting non-equilibrium flow solver is developed based on 5-species air chemistry and recent thermal property models. It is being applied to DNS of strong shock and turbulence interactions. The main shock is treated by the shock-fitting method as a sharp boundary of the computational domain. The rest of weak or secondary shocks induced by interactions of the main shock and freestream disturbance are captured by shock-capturing methods. The code is implemented based on a two-temperature model. It is assumed that translational and rotational energy modes are in equilibrium at the translational temperature whereas vibration energy, electronic energy, and free electron energy are in equilibrium at the vibration temperature. The code has been tested on a case of non-equilibrium reacting flow over a cylinder. Although no numerical result is yet obtained for strong shock and turbulence problem at high shock Mach number with real gas effects, due to the tremendous cost of computer resources, this paper shows that our shock-fitting code is capable of solving strong shock and turbulence interaction problems with high-order accuracy.

Acknowledgement

The research was supported partially by DOE office of Science as part of a SciDAC project with “Science Application” in Turbulence and partially by the AFOSR/NASA National Center for Hypersonic Research in Laminar-Turbulent Transition. The authors

appreciate helps from Dr. Peter A. Gnoffo and Dr. Helen C. Yee on the test case. Numerical simulations are mainly run on TeraGrid resources provided by TACC under grant number TG-ASC100002 supported in part by the National Science Foundation. The views and conclusions contained herein are those of the authors and should not be interpreted as necessarily representing the official policies or endorsements either expressed or implied, of the Air Force Office of Scientific Research or the U.S. Government.

Reference

1. Vincenti, W.G., and Kruger Jr., C. H., *Introduction to Physical Gas Dynamics* 1967: Krieger Publishing Co, INC.
2. Mannella, G.G., *Chemical Reactions in Electrical Plasmas.* The OHIO Journal of Science, 1966. **66**(3): p. 334-339.
3. Rawat, P.S., and Zhong, X., *On high-order shock-fitting and front-tracking schemes for numerical simulation of shock–disturbance interactions.* Journal of Computational Physics, 2010. **229**(19): p. 6744-6780
4. Lee, T.K., and Zhong, X., *Spurious numerical oscillations in simulation of supersonic flows using shock-capturing schemes.* AIAA Journal, 1999. **37**(3): p. 313-319.
5. Hash, D., Olejniczak, J, Wright, M. J., Dinish, P., Pulsonetti, M., Hollis, B. R., Gnoffo, P. A., Barnhard, M., Nompelis, I., and Candler, G., *FIRE II Calculations for Hypersonic Nonequilibrium Aerothermodynamics Code Validation: DPLR, LAURA, and US3D*. 2007, AIAA 2007-0605.
6. Johnsen, E., Larsson, J., Bhagatwala, A. V., Cabot, W. H., Moin, P., Olson, B. J., Rawat, P. S., Shankar, S. K., Sjögreen, B., Yee, H. C., Zhong, X., and Lele, S. K., *Assessment of high-resolution methods for numerical simulations of compressible turbulence with shock waves.* Journal of Computational Physics, 2010. **229**(4): p. 1213-1237.
7. Kovasznay, L.S.G., *Turbulence in supersonic flow*. Journal of the Aeronautical Sciences, 1953. **20**(10): p. 657-682.
8. Moore, F.K., *Unsteady oblique interaction of a shock wave with a plane disturbances.* NACA TN-2879 (Also as NACA Rep. 1165), 1953.
9. Kerrebrock, J.L., *The interaction of flow discontinuities with small disturbances in a compressible fluid.* PhD thesis, California Institute of Technology, 1956.
10. Goldstein, M.E., *Turbulence generated by the interaction of entropy fluctuations with non-uniform mean flows.* Journal of Fluid Mechanics, 1979. **93**: p. 209-224.
11. Lee, L., Moin, P., and Lele, S. K., *Interaction of isotropic turbulence with a shock wave.* Report TF-52. Dept. Mech. Eng., Stanford Univ., CA, 1992.
12. Lee, L., Lele, S. K., and Moin, P., *Direct numerical simulation of isotropic turbulence interacting with a weak shock wave.* Journal of Fluid Mechanics, 1993. **251**: p. 533-562.
13. Mahesh, K.A., Lee, L., Lele, S. K., and Moin, P., *The interaction of an isotropic field of acoustic waves with a shock wave.* Journal of Fluid Mechanics, 1995. **300**: p. 383-407.

14. Mahesh, K.A., Lele, S. K., and Moin, P., *The influence of entropy fluctuations on the interaction of turbulence with a shock wave.* Journal of Fluid Mechanics, 1997. **334**: p. 353-379.
15. Fabre, D., Jacquin, L., and Sesterhenn, J., *Linear interaction of a cylindrical entropy spot with a shock.* Journal of Physics of Fluids A, 2001. **13**(8): p. 2403-2422.
16. Pao, S.P., and Salas, M. D., *A numerical study of two-dimensional shock vortex interaction.* AIAA Paper 81-1205, 1981.
17. Zang, T.A., Hussaini, M. Y., and Bushnell, D. M. , *Numerical Computations of Turbulence Amplification in Shock-Wave Interactions.* AIAA Journal, 1984. **22**(1): p. 13-21.
18. Hussaini, M.Y., Kopriva, D., Salas, M. D., and Zang, T. A., *Spectral methods for the Euler equations. II - Chebyshev methods and shock fitting.* AIAA Journal, 1987. **23**: p. 234-240.
19. Meadows, K.R., Kumar, A., and Hussaini, M. Y., *Computational Study on the Interaction between a vortex and a shock Wave.* AIAA Journal, 1991. **29**(2): p. 174-179.
20. Meadows, K.R., and Casper, J., *Computing unsteady shock waves for aeroacoustic applications.* AIAA Paper 1993-4329, 1993.
21. Grasso, F., and Pirozzoli, S. , *Shock-wave-vortex interactions: shock and vortex deformations, and sound production.* Theoretical and Computational Fluid Dynamics, 1993. **13**(6): p. 421-456.
22. Andreopoulos, Y., Agui, J. H., and Briassulis, G., *Shock wave-turbulence interactions.* Annual Review of Fluid Mechanics 2000. **32**: p. 309-345.
23. Hannappel, R., and Friedrich, R., *Direct numerical simulation of a Mach 2 shock interacting with isotropic turbulence.* Applied Scientific Research, 1995. **54**: p. 205-221.
24. Jamme, S., Cazalbou, J. B., Torres, F., and Chassaing, P., *Direct numerical simulation of the interaction between a shock wave and various types of isotropic turbulence.* Flow, Turbulence and Combustion, 2202. **68**: p. 227-268.
25. Adams, N.A., and Shariff, K., *A high-resolution hybrid compact-ENO scheme for shock turbulence interaction problems.* Journal of Computational Physics, 1996. **127**(27): p. 57-.
26. Adams, N.A., and Shariff, K., *Direct numerical simulation of turbulent compression corner flow.* Theoretical and Computational Fluid Dynamics, 1998. **12**: p. 109-129.
27. Pirozzoli, S., *Conservative hybrid compact-WENO schemes for shock-turbulence interaction.* Journal of Computational Physics, 2002. **178**(1): p. 81-117.
28. Ducros, F., Ferrand, V., Nicoud, F.,Weber, C., Darracq, D., Gacherieu C., and Poinsot, T., *Large eddy simulation of the shock/turbulence interaction.* Journal of Computational Physics, 1999. **152**: p. 517-549.
29. Agui, J.H., *Shock wave interactions with turbulence and vortices*. 1998, PhD Thesis, City University of New York: New York.
30. Lele, S.K., and Larsson, J., *Shock-turbulence interaction: What we know and what we can learn from peta-scale simulations.* Journal of Physics: Conference Series, 2009. **180**(012032).

31. Rawat, P.S., and Zhong, X. *High- Order Shock-Fitting and Front-Tracking Methods for Numerical Simulation of Shock- Disturbance Interactions*. in *AIAA paper 2009-1138*. 2009.
32. Casper, J., and Carpenter, M. H., *Computational Considerations for the Simulation of Shock-Induced Sound.* SIAM Journal of Scientific Computing, 1998. **19**(3): p. 813-828.
33. Rawat, P.S., and Zhong, X., *Direct Numerical Simulations of Turbulent Flow Interactions with Strong Shocks Using Shock-Fitting Method.* AIAA paper 2011-649, 2011.
34. Zhong, X., *High-order finite-difference schemes for numerical simulation of hypersonic boundary-layer transition.* Journal of Computational Physics, 1998. **144**: p. 662-709.
35. Lee, L., Lele, S. K., and Moin, P., *Simulation of spatially evolving compressible turbulence and the applicability of Taylor's Hypothesis.* Physics of Fluids A, 1992. **4**: p. 1521-1530.
36. Gupta, R.N., Yos, J. M., Thompson, R. A., and Lee, K-P., *A Review of Reaction Rates and Thermodynamic and Transport Properties for an 11-Species Air Model for Chemical and Thermal Nonequilibrium Calculations to 30 000 K*. 1990, NASA Reference Publication 1232.
37. Gnoffo, P.A., Gupta, R. N., and Shinn, J. L., *Conservation equations and physical models for hypersonic air flows in thermal and chemical nonequilibrium*. 1989, NASA Technical Paper 2867.
38. Erlebacher, G., Hussaini, Y., Kreiss, H. O., and Sarkar, S., *The Analysis and Simulation of Compressible Turbulence.* Theoretical and Computational Fluid Dynamics, 1990. **2**: p. 73-95.
39. Larsson, J., and Lele, S.K., *Direct numerical simulation of canonical shock/turbulence interaction.* Physics of fluids, 2009. **21**(12): p. 126101-126101-12.